

Detection of Hard X-Rays from the Compton-Thick Seyfert 2 Galaxy NGC 2273 with Suzaku

Hisamitsu AWAKI,¹ Yuichi TERASHIMA,¹ Yuusuke HIGAKI,¹ Yasushi FUKAZAWA,²

¹*Department of Physics, Ehime University, Matsuyama, 790-8577, Japan*

²*Department of Physical Science, Hiroshima University,*

1-3-1 Kagamiyama, Higashi-Hiroshima, Hiroshima 739-8526

awaki@astro.phys.sci.ehime-u.ac.jp

(Received 0 0; accepted 0 0)

Abstract

We have obtained a broad-band spectrum of the Compton-thick Seyfert 2 galaxy NGC 2273 with Suzaku. The spectrum reveals the first detection of hard X-rays above ~ 10 keV from NGC 2273. The broad-band spectrum is well represented by a three-component model, accompanied by both a strong iron $K\alpha$ line with an equivalent width of ~ 1.8 keV and several weak lines. The three-component model consists of a soft component, a reflection component from cold matter, and an absorbed power-law component. The soft component can be represented by thin thermal emission with $kT \sim 0.56$ keV or by a scattered component with a scattering fraction of 0.4%. Fixing the photon indices of the power law and reflection components at 1.9, we found that the power law component, heavily absorbed by gas with a column density of $\sim 1.5 \times 10^{24}$ cm $^{-2}$, has an intrinsic 2–10 keV luminosity of $\sim 1.7 \times 10^{42}$ erg s $^{-1}$. We also apply a reflection model based on a Monte Carlo simulation, assuming a simple torus geometry. We found that the model fits the broad band spectrum well, and we place some tentative constraints on the geometry of the putative torus in NGC2273.

Key words: galaxies:active—galaxies: Seyfert —galaxies: individual (NGC 2273)

1. Introduction

Compton-thick active galactic nuclei (AGN) are predicted to constitute about a half of AGN (e.g., Risaliti et al. 1999). This type of AGN has a characteristic strong iron line with an equivalent width of > 1 keV (e.g., Bassani et al. 1999), and a low ratio of $L_X/L_{[\text{OIII}]}$ (e.g., Maiolino et al. 1998), where L_X and $L_{[\text{OIII}]}$ are the luminosity in the 2–10 keV band and the luminosity of the $[\text{OIII}]\lambda 5007$ line, respectively. However, the detailed nature of this type of AGN remains unclear due to the heavy obscuration below 10 keV and the complex X-ray spectrum. To reveal the nature of the hidden nucleus and to understand the complex X-ray

spectra, we need to obtain broad-band spectra covering energies above 10 keV. BeppoSAX detected hard X-rays above 10 keV from several Compton-thick Seyfert 2 galaxies: e.g., NGC 1068 (Matt et al. 1997), NGC 4945 (Guainazzi et al. 2000), Mrk 3 (Cappi et al. 1999), Circinus galaxy (Matt et al. 1999), NGC 3393, and NGC 4939 (Maiolino et al. 1998). Thanks to observations above 10 keV with INTEGRAL, Swift/BAT, and Suzaku, the number of detected Compton-thick sources has increased to 18 (Della Ceca 2008, and references therein). However, the number of Compton-thick sources whose wide-band spectra were analyzed in detail is small: e.g., NGC 1068 (Matt et al. 1997), Circinus galaxy (Matt et al. 1999; Yang et al. 2008), Mrk 3 (Cappi et al. 1999; Awaki et al. 2008), NGC 4945 (Guainazzi et al. 2000; Itoh et al. 2008), and ESO 005-G004 (Ueda et al. 2007).

NGC 2273 is a nearby SB(r)a galaxy with a Seyfert 2 nucleus ($z=0.006138$), and it is listed in a bright [OIII] sample of Risaliti et al. (1999). This galaxy is considered to be a Compton-thick Seyfert 2 galaxy due to the detection of a strong iron line with an equivalent width of greater than 1 keV and a low ratio of $L_X/L_{[\text{OIII}]}$ (e.g., Guainazzi et al. 2005). The existence of a hidden nucleus is also suggested by the detection of polarized broad lines (Moran et al. 2000), establishing the presence of a Seyfert 1 nucleus obscured by thick matter. To measure the absorbing column, NGC 2273 was observed with ASCA, BeppoSAX, and XMM-Newton, but the column density could not be determined from these data. Terashima et al. (2002) found that NGC 2273 had a large column density of $1.1 \times 10^{24} \text{ cm}^{-2}$, by fitting the 0.8–10 keV ASCA spectra with a partially-covered power-law model. On the other hand, Maiolino et al. (1998) and Guainazzi et al. (2005) suggested a large absorbing column $>10^{25} \text{ cm}^{-2}$, due to lack of the absorbed power-law component in the spectra below 10 keV observed with BeppoSAX and XMM-Newton. In order to measure the column density and to reveal its nuclear activity, a wide-band spectrum of NGC 2273 is crucial.

Using the Japanese X-ray satellite Suzaku, it is possible to obtain a wide-band spectrum from 0.2 to 700 keV (Mitsuda et al. 2007). The satellite is suitable for achieving the aims of detecting the high energy X-rays above 10 keV and of revealing the properties of the NGC 2273 nucleus. In this paper, we present the analysis of the broad-band spectrum of NGC 2273 obtained with Suzaku, and present the results by fitting the spectrum with a baseline model consisting of a soft component, an absorbed power-law component, and a reflection component. In addition, we apply a reflection model based on a Monte Carlo simulation assuming a simple torus geometry (Ikeda et al. 2008). Quoted errors correspond to the 90 % confidence level for one interesting parameter, unless explicitly stated.

2. Observations and Data Reduction

NGC 2273 was observed with the Suzaku satellite on 2007 April 21–22 during the AO-2 phase. Suzaku has four X-ray telescopes (XRTs: Serlemitsos et al. 2007) with X-ray CCD cameras (XIS) in their focal-planes. The XISs are sensitive to 0.2–12 keV X-rays on a $18' \times 18'$

field of view. Three of the four XISs (XIS-0, 2, and 3) are front-illuminated CCDs (FI) and the other XIS (XIS-1) is a back-illuminated CCD (BI) (Koyama et al. 2007). Due to damage to XIS2 on 2006 November 9, no astronomical data were obtained with XIS2. Suzaku also has a non-imaging hard X-ray detector (HXD: Takahashi et al. 2007). The HXD has two types of detectors, the PIN and the GSO, which are sensitive between ~ 10 and ~ 700 keV.

NGC 2273 was placed at the HXD-nominal position, and then both XIS and HXD data were obtained simultaneously. The XISs were operated in the normal clocking mode with spaced-raw-charge injection (SCI) in order to recover the cumulative effect of in-orbit radiation damage (Nakajima et al. 2008). The observed data were processed through pipeline processing. We analyzed the v2.0 data by using the analysis software package HEASOFT 6.4 and the calibration database CALDB released on 2008 February 1.

2.1. XIS Reduction

The XIS team recommends a recalculation of the PI values to account for the update of the CALDB files. Thus, we performed the recalculation of unfiltered event files, and then reprocessed the cleaned event files from the XIS-0, 1, and 3 with the *xselect* script provided by NASA/GSFC GOF ¹. We imposed an additional data screening with a criterion "COR > 6", where COR is geomagnetic cut-off rigidity in units of GV. The net exposure of the cleaned event data was about 76 ks. We made a 0.4–2 keV band image and a 2–10 keV band image using the cleaned XIS data (Figure 1), and clearly detected NGC 2273 and two nearby bright X-ray sources, 2XMM J065012.9+604842 and 2XMM J065003.7+604639. The XIS0 count rates of these detected sources are listed in Table 1. The former bright XMM-source is also known as a radio source NVSS J065012+604842 (Condon et al. 1998). Since one of the serendipitous X-ray sources, 2XMM J065012.9+604842 is within $\sim 2'$.1 of NGC 2273, we selected X-ray events within a $2'$.0 radius centered on NGC 2273 and removed X-ray events close to the serendipitous source for the spectral analysis in order to reduce the contamination from the serendipitous X-ray source.

Response matrices (RMFs) and ancillary response files (ARFs) were generated for each XIS independently by using *xisrmfgen* and *xissimarfgen* (Ishisaki et al. 2007). To examine the accuracy of the energy scale of our data, we extracted spectra of the ⁵⁵Fe calibration sources which illuminate the CCD corners, and then fitted the spectra with a two-Gaussian model. The difference between the best-fit center energies of the calibration sources and the weighted value of the theoretical energies for the transitions of $K\alpha_1$ and $K\alpha_2$ was 0–10 eV, which was within the accuracy ($\sim 0.2\%$ at Mn- $K\alpha$) of the energy calibration of XIS. The line widths of the calibration sources were found to be < 25 eV. Since the energy scales of the front-illuminated CCDs, XIS-0 and 3 were quite similar to within 5 eV, we added the XIS-0 and XIS-3 spectra

¹ The Suzaku Data Reduction Guide January 2008, which can be obtained from the GOF web page at http://heasarc.gsfc.nasa.gov/docs/suzaku/aehp_data_analysis.html

of NGC 2273 using *mathpha*.

To estimate the contamination from the nearby source, we made a spectrum of 2XMM J065012.9+604842 by extracting X-ray events within a $2'$ radius centered on this source. Note that the X-ray events close to NGC 2273 were removed in this spectral analysis. The X-ray spectrum is shown in Figure 2. The spectrum was fitted by a single power law model with a photon index of $1.72^{+0.15}_{-0.14}$ absorbed by $N_{\text{H}}=7^{+7}_{-6}\times 10^{20}$ cm^{-2} . The absorbing column is consistent with the Galactic column density toward NGC 2273, 6.7×10^{20} cm^{-2} (Kalberla et al. 2005). The X-ray fluxes in the 0.5–2 keV and the 2–10 keV bands were measured to be 7.6×10^{-14} and 1.7×10^{-13} $\text{ergs s}^{-1} \text{cm}^{-2}$, respectively. We found, analyzing the XMM-Newton archival data, that the flux had increased by a factor two in both bands. The contamination of 2XMM J065012.9+604842 in the NGC 2273 source region was inferred to be $\sim 1.8\times 10^{-14}$ $\text{erg s}^{-1} \text{cm}^{-2}$ in the 2–10 keV band, and this contamination was taken into account in our fitting procedure.

2.2. HXD Reduction

The internal (non-X-ray) background (NXB) of the HXD-PIN is variable, and depends strongly on the Suzaku satellite orbit (Kokubun et al. 2007). Thus we extracted both the source and the NXB spectra with identical good time intervals. After the instrument dead-time correction of the source spectrum, an exposure time of 64.6 ks was obtained. A NXB spectrum for the NGC 2273 observation was produced by the tuned NXB event file for v2.0 data. Since the HXD-PIN is not an imaging detector, we also had to subtract any contribution from the Cosmic X-ray Background (CXB). We simulated a CXB spectrum observed by the HXD-PIN, and then added the simulated CXB spectrum to the NXB spectrum. The HXD-PIN count rate of NGC 2273 was found to be about 0.020 ± 0.002 cts s^{-1} in the 15–40 keV band, which was about 7% of the NXB of the HXD-PIN. Note that the errors presented in this subsection are at 1σ level. The accuracy of the present PIN NXB model in a 40 ks observation is about 1% of the NXB at the 1σ level (Mizuno et al. 2008²). NGC 2273 was detected in the 15–40 keV band with $> 5\sigma$ level. We confirmed the detection of the hard X-rays of NGC 2273 from the comparison of the PIN count rates in the 15–40 keV band with those obtained during earth occultation. Although there were no earth occultation data taken during this observation, we were able to use the earth occultation data from both the previous and the subsequent observations; these are included in the Suzaku trend archive provided by the Suzaku team. The upper panel of Figure 3 shows a light curve of the PIN count rates in the 15–40 keV band during earth occultation and the data reproduced by the NXB model. We also plotted the light curve of NGC 2273 in this panel. The bottom panel shows the light curve in which the NXB model has been subtracted. A clear excess was found during the NGC 2273 observation with a mean count rate of 0.035 ± 0.003 c s^{-1} . Subtracting the CXB count rate of 0.016 c s^{-1} from the mean count rate yields an estimated net count rate of 0.019 ± 0.003 c s^{-1} . Since the PIN FOV is $34'\times 34'$

² <http://www.astro.isas.jaxa.jp/suzaku/doc/suzakumemo/suzakumemo-2008-03.pdf>

(Kokubun et al. 2007), there are bright X-ray sources detected with XIS in the PIN FOV. We estimated the contamination of the brightest XMM source, 2XMM J065012.9+604842 by extrapolation of its 2-10 keV band spectrum. The contamination was estimated to be about 0.0005 c s^{-1} in the 15–40 keV band, which corresponds to about 3 % of the net count rate. Since the 2–10 keV count rate of the other XMM source is about 1/3 of the brightest XMM source, we concluded that NGC 2273 was detected in the 15–40 keV band.

The response matrix for a point source at the HXD nominal position (ae_hxd_pinhxnome3_20070914.rsp) was used for our spectral analysis. The cross-normalization of the HXD-PIN relative to the XIS0 have been derived using Suzaku observations of the Crab nebula. We used the cross-normalization of 1.137 ± 0.015 at the HXD nominal position (Ishida et al. 2007³).

The spectra of XIS and HXD PIN were binned to a minimum of 50 and 1500 counts per bin, respectively.

3. Analysis & Results

3.1. Spectral Analysis with the Baseline Model

Guainazzi et al. (2005) found that the XMM-Newton spectrum was well fitted with a thin-thermal model (*mekal* in *XSPEC*), plus Compton reflection model (*pe xrav*). Thus we fitted the XIS and HXD spectra with this model using *XSPEC* v12.4.0. The abundances of Anders & Grevesse (1989) were used. The cosine of the inclination and the iron abundance in *pe xrav* were fixed at 0.45 and one solar abundance, respectively. The best-fit spectrum and residuals are shown in Figure 4. The overall spectrum was represented by this model with a χ^2 of 199.2 with 130 degrees of freedom (d.o.f.); however, there were several features apparent in the residuals. Therefore, we added gaussian components at ~ 0.7 , ~ 1.8 , ~ 3.2 , ~ 7.0 , and ~ 7.2 keV to the model. The χ^2 was reduced to 120 with 120 d.o.f. The best-fit parameters are listed as Model 1 in Table 2. The ~ 3.2 keV line like feature was also detected in the BeppoSAX observation (Maiolino et al. 1998), although the significance of this feature was low. The best-fit photon index was well determined to be $1.49^{+0.13}_{-0.08}$, which was consistent with that found in the XMM-Newton spectrum (1.5 ± 0.4 ; Guainazzi et al. 2005). The thin-thermal component was represented by a temperature of $kT \sim 0.59$ keV and a metal abundance of 0.04 solar. We note that a portion of the line fluxes of the additional lines at ~ 0.7 and ~ 1.8 keV could be explained by increasing metal abundances of O and Si to $0.1^{+0.4}_{-0.1}$ and $0.45^{+0.30}_{-0.20}$ solar, respectively. However, line-like features still remained near these line energies. This may indicate that the lines are composed of different origins. The thermal component is absorbed by a thick matter with $N_{\text{H}} = (2.9^{+2.6}_{-1.4}) \times 10^{21} \text{ cm}^{-2}$, which is significantly larger than the Galactic column density. The observed fluxes in the 0.5–2 keV, 2–10 keV, and 15–40 keV bands were estimated to be

³ <http://www.astro.isas.jaxa.jp/suzaku/doc/suzakumemo/suzakumemo-2007-11.pdf>

6×10^{-14} , 9.5×10^{-13} , and 1.0×10^{-11} erg s $^{-1}$ cm $^{-2}$, respectively. The 2–10 keV flux is nearly equal to the BeppoSAX result (Maiolino et al. 1998), although the flux is 1.3 times larger than that of XMM-Newton. The 0.5–2 keV flux is consistent with the XMM-Newton result considering the uncertainties (Guainazzi et al. 2005). The iron line intensity of $(2.5\pm 0.2)\times 10^{-5}$ ph s $^{-1}$ cm $^{-2}$ is consistent with that found using XMM-Newton ($(2.3_{-0.3}^{+0.4})\times 10^{-5}$ ph s $^{-1}$ cm $^{-2}$) and using BeppoSAX ($(2.36_{-0.70}^{+1.35})\times 10^{-5}$ ph s $^{-1}$ cm $^{-2}$).

The best-fit photon index in the above model was clearly smaller than the canonical value of ~ 1.9 for AGNs (e.g., Nandra et al. 1997). Therefore, we added a heavily absorbed component to the model. We assumed that the photon index of the absorbed power-law component is the same as that of the reflection component, and fixed the photon index at 1.9. The model gives a χ^2 value of 119 with 120 d.o.f. The best-fit parameters are listed in Tables 2 and 3, and residuals are plotted in Figure 4 (Model 2 in Table 2). Since the best-fit absorption column (N_{H}) was deduced to be $(1.46\pm 0.42)\times 10^{24}$ cm $^{-2}$, we considered attenuation of the X-ray light due to Thomson scattering by the thick matter along our line of sight. The reflection ratio R of the cold reflection to the absorbed power law component was found to be $0.5_{-0.3}^{+0.7}$. The 2–10 keV intrinsic luminosity, L_{2-10} , was estimated to be $1.7_{-0.4}^{+2.5}\times 10^{42}$ erg s $^{-1}$ assuming $H_0=70$ km s $^{-1}$ Mpc $^{-1}$. The error of the luminosity was calculated from the error on the normalization of the absorbed power-law component. The equivalent width (hereafter EW) of the iron K α line with respect to the continuum emission was deduced to be 1.8 ± 0.1 keV. The column density and the reflection ratio are affected by the systematic uncertainties of the reproducibility of the PIN NXB. For the +1% NXB and -1% NXB, the best-fit values became 1.0 and 0.3 for R , and 1.15×10^{24} cm $^{-2}$ and 1.72×10^{24} cm $^{-2}$ for N_{H} , respectively. The change in these parameters is smaller than the statistical errors on R and N_{H} .

N_{H} and L_{2-10} are expected to depend on the intrinsic power-law photon index. We examined this parameter coupling by fitting the spectrum with model 2 assuming a photon index of 1.7 or 2.1 instead of 1.9. The models using these photon indices also fit well with $\chi^2=116$ and 124 (120 d.o.f), respectively. For a photon index of 1.7, N_{H} and L_{2-10} were found to be $1.10_{-0.40}^{+0.55}\times 10^{24}$ cm $^{-2}$ and $0.5_{-0.2}^{+1.0}\times 10^{42}$ erg s $^{-1}$, respectively. On the other hand, for a photon index of 2.1, N_{H} and L_{2-10} were found to be $1.6\pm 0.4\times 10^{24}$ cm $^{-2}$ and $3.0_{-1.5}^{+1.7}\times 10^{42}$ erg s $^{-1}$, respectively. These best-fit values of N_{H} are close to those obtained with the photon index was fixed at 1.9; in contrast, the L_{2-10} values are different from that using a photon index of 1.9. Levenson et al. (2006) found a relationship between Fe line luminosity L_{Fe} and intrinsic luminosity based on Monte Carlo simulations. Although the ratio L_{Fe}/L_{2-10} depends on the geometry of a torus, they found a typical ratio of 2×10^{-3} . NGC 2273 has a intense iron line with $L_{\text{Fe}}\sim 2\times 10^{40}$ erg s $^{-1}$, and the intense iron line requires $L_{2-10}\sim 10^{43}$ erg s $^{-1}$. Based on the Levenson et al. (2006) relationship, the L_{2-10} found using a photon index of 1.7 may be too low to explain the observed L_{Fe} .

It is possible to search for a Compton shoulder (hereafter CS) on an iron K α line with

large equivalent width. We added a pulse function with a pulse width of 156 eV in order to represent the first-order CS of iron $K\alpha$ line (Awaki et al. 2008). We found that the fraction of the CS intensity with respect to that of the primary Gaussian component is less than 15%. Matt (2002) calculated the fractions of CS for a spherical distribution of matter, and for a plane-parallel slab. The low fraction of $< 15\%$ indicates a low column density below 10^{24} cm^{-2} and/or small inclination angle to the slab.

An iron $K\beta$ line was also detected with an intensity of $(3.2 \pm 1.0) \times 10^{-6} \text{ ph s}^{-1} \text{ cm}^{-2}$. Fe $K\alpha$ and $K\beta$ lines are useful for estimating the ionization state of the line-emitting gas (e.g., Bianchi et al. 2005; Yaqoob et al. 2007). We derived a line intensity ratio, $I_{K\beta}/I_{K\alpha}$, of 0.13 ± 0.04 , which is consistent with emission by low ionization states of iron (Palmeri et al. 2003). The measured center energies of the iron $K\alpha$ and $K\beta$ lines also indicate a low ionization state ($\leq \text{Fe IX}$) of the reflecting matter. The low ionization state corresponds to an ionization parameter ($\xi = \frac{L^{\text{ion}}}{n r^2}$) of $\xi < 1 \text{ erg cm s}^{-1}$, assuming low density gas, where L^{ion} , n and r are the luminosity in the 1 – 1000 ryd band, the hydrogen density of material, and the distance from the X-ray source. Assuming a simple power law model with a photon index of 1.9, L^{ion} is inferred to be 3.5-times the 2–10 keV luminosity.

The soft component of NGC 2273 was fitted with a thermal plasma model with $kT \sim 0.56$ keV. Next, we examined whether the soft component instead could be represented by a scattered component as seen in Mrk 3. Since the soft component of Mrk 3 is a good template for the scattered light of AGN (e.g., Sako et al. 2000), we rescaled the soft component of Mrk 3 to produce the soft component of NGC 2273. In this fit, we fixed the photon index at 1.8, which is the best-fit photon index for Mrk 3 (Awaki et al. 2008). We found that the overall spectrum of NGC 2273 could be represented with a scaling factor of ~ 0.092 . The best-fit parameters are listed as model 3 in Table 2, and the best-fit spectrum is shown in Figure 5. The scaling factor corresponds to a scattered fraction of $0.4 \pm 0.1\%$. Note that we also included additional lines that are present in the thin thermal model. The best-fit line intensities for the 0.7 keV and 1.8 keV lines are changed to $7_{-4}^{+7} \times 10^{-6}$ and $1.2 \pm 10^{-6} \text{ ph s}^{-1} \text{ cm}^{-2}$, respectively.

3.2. Spectral Analysis with a Reflection Model based on a Monte Carlo Simulations

The baseline model is useful to reproduce X-ray spectra of Seyfert 2 galaxies empirically. However, it is difficult to obtain information about the structure of surrounding material from the spectral fitting with the baseline model, since *pe xrav* was developed for an accretion disc geometry (Magdziarz & Zdziarski 1995). Thus, we tried to reproduce the X-ray spectrum of NGC 2273 with a reflection model based on a Monte Carlo simulation in which a simple torus geometry of the surrounding material with arbitrary half opening angle, viewing angle, and column density along the equatorial plane was assumed (see Figure 2 in Ikeda et al. 2008). Ikeda et al. (2008) divided the simulation spectra into three components: the direct component, a reflection component absorbed by the torus itself (reflection 1), and an unabsorbed reflection

component (reflection 2), and created table models of these reflection components for XSPEC. We fitted the observed spectrum with these table models in the energy range from 1 to 40 keV (model 4 in Table 4). These models also worked well with a χ^2 of 108 (dof=106) (see Table 4 and Figure 6). Due to Compton scattering by thick matter along our line of sight, the absorbed component in Figure 6 was reduced by a factor of $\exp(-\sigma_c N_H)$, where σ_c is the Compton scattering cross-section. Ikeda et al. (2008) pointed out that the χ^2 value was affected by the statistical deviation of the table models. In the case of Mrk 3, the scatter in χ^2 due to that deviation was estimated to be about 5. Since NGC 2273 is fainter than Mrk 3, the scatter of the χ^2 was estimated to be less than 1. The best-fit opening angle of the torus was found to be $40_{-30}^{+25^\circ}$. We found that the viewing angle was strongly coupled to the opening angle, and the best-fit viewing angle was 2–3° larger than the opening angle. In Table 4, we give the difference between these angles when we fixed the opening angle at the best-fit value. This result means that we observe the nucleus along a line of sight intercepting the torus near its edge. As a result, we observed strong unabsorbed reflection. The best-fit photon index of the power-law component is $2.42_{-0.57}^{+0.08}$. The positive bound on the photon index is a consequence of the hard limit of the table models of $\Gamma = 2.5$. The column density along the equatorial plane of the torus is $5.4_{-3.1}^{+3.7} \times 10^{24} \text{ cm}^{-2}$. The X-ray luminosity in the 2–10 keV band was estimated to be $3.9 \times 10^{42} \text{ erg s}^{-1}$. When we fixed the photon index at 1.9, the χ^2 becomes 111.6 (dof=107), the column density along the equatorial plane becomes $(4.8_{-3.0}^{+5.2}) \times 10^{24} \text{ cm}^{-2}$ and the intrinsic X-ray luminosity in the 2–10 keV band is estimated to be $1.9 \times 10^{42} \text{ erg s}^{-1}$.

4. Discussion

4.1. Hard X-ray Emission and AGN Activity

Thanks to the high sensitivity of Suzaku, we detected X-ray photons above 10 keV at the $> 5 \sigma$ significance level. The hard X-ray flux in the 15–40 keV band was estimated to be $1 \times 10^{-11} \text{ erg s}^{-1} \text{ cm}^{-2}$. The wide-band X-ray spectrum in the 0.3–40 keV band was roughly fitted with the model applied by Guainazzi et al. (2005). However, we found that the best-fit photon index of ~ 1.5 is clearly smaller than the canonical value for Seyfert galaxies. Therefore, we added an absorbed power-law emission to the model, and obtained the best-fit absorption column of $\sim 1.5 \times 10^{24} \text{ cm}^{-2}$, and the intrinsic luminosity of $L_{2-10} = 1.7 \times 10^{42} \text{ erg s}^{-1}$. Our observation has revealed a luminous nucleus obscured by optically thick matter.

We compared the intrinsic X-ray luminosity of NGC 2273 with the [OIII] $\lambda 5007$ luminosity in order to determine the nature of the Compton-thick nucleus. Heckman et al. (2005) shows that ratios of hard X-ray (2–10 keV) to [OIII] luminosities for Seyfert 1 galaxies are distributed around 1.59 dex with a standard deviation of only 0.48 dex. The [OIII] luminosity of NGC 2273 was found to be $4.2 \times 10^{40} \text{ erg s}^{-1}$ by Whittle (1992) assuming $H_0 = 70 \text{ km s}^{-1} \text{ Mpc}^{-1}$. Based on the mean ratio given by Heckman et al. (2005), this [OIII] luminosity

suggests that the intrinsic X-ray luminosity from the AGN should be 1.6×10^{42} erg s⁻¹ in the 2–10 keV band. This estimate is consistent with our result. Thus, the ionized region emitting the [OIII] line is most likely powered by the intense emission from the nucleus. Maiolino et al. (1998) pointed out that the Seyfert 2 galaxy NGC 2273 was consistent with being Compton thick because of its low luminosity ratio, $L_{2-10}/L_{[\text{OIII}]}$, of < 0 dex. Our Suzaku observation allows us to measure the 2 - 10 keV intrinsic luminosity of NGC 2273, and suggests that NGC 2273 has a similar intrinsic ratio as those of Seyfert 1 galaxies.

We note that NGC 2273 was undetected in a 12 ks observation by the PDS on-board BeppoSAX (Maiolino et al. 1998). They obtained a 1σ -upper limit of 0.096 c s⁻¹ in the 15-100 keV band, which corresponds to a 15-40 keV flux of $\sim 5 \times 10^{-12}$ erg s⁻¹ cm⁻², assuming the same spectral shape as that of Mrk 3. This upper limit is about half of our detected flux. This discrepancy can be explained by time variability of the absorbed power-law emission on a time scale of years. If NGC 2273 lacked the absorbed power-law emission, the observed flux would be reduced to $\sim 5 \times 10^{-12}$ erg s⁻¹ cm⁻². The absence of the absorbed emission may be caused by a decrease of the intrinsic luminosity and/or an increase of the absorption column up to $> 3.5 \times 10^{24}$ cm⁻².

4.2. Soft X-ray Emission

Ferruit, Wilson, & Mulchaey (2000) found [NII] + H α emission associated with a nuclear ring, and this emission was inferred to be produced by star-formation activity in the ring. The soft X-rays represented by a thin-thermal model with $kT \sim 0.6$ keV may be associated with the star-formation activity. The X-ray luminosity, $L_{0.5-2.0}$, of the thin-thermal component was estimated to be 6×10^{39} erg s⁻¹ in the 0.5 – 2.0 keV band. This galaxy has luminous far-infrared emission with $L_{\text{FIR}} = 2.9 \times 10^{43}$ erg s⁻¹ (Lonsdale et al. 1992). The observed 0.5–2 keV luminosity is nearly equal to expectations given the ratio of $L_{0.5-2.0}/L_{\text{FIR}}$ for starburst galaxies (Ranalli et al. 2002). In the thin-thermal model, the absorption by $N_{\text{H}} = (2.9^{+2.6}_{-1.4}) \times 10^{21}$ cm⁻² is required. The absorption can be explained by an obscuration of HII regions in the galaxy ring (Ferruit et al. 2000). On the other hand, the soft X-rays may come from a photoionized region as often seen in other Seyfert 2 galaxies. The scattering fraction is found to be $\sim 0.4\%$, which is about half that found in Mrk 3 (Awaki et al. 2008). In this model, the additional lines at ~ 0.7 keV and ~ 1.8 keV were explained by the emission from photo-ionized plasma. The line at ~ 1.8 keV suggests a lower-ionization form of Si in the photoionized region of NGC 2273 compared with that of Mrk 3.

Since the observed soft emission is consistent both with thin thermal emission from the star-forming region, and with a scattered component often seen in Seyfert 2 galaxies, we cannot conclusively determine its origin. A deep Chandra observation could possibly separate the thin thermal emission from the nuclear emission, since the H α region is often coincident with the thin-thermal emission region, and the diameter of the circumnuclear region is about $4''$.

4.3. Implications for reflecting matter in NGC 2273

Using the iron lines, we found the reflecting matter is in a low ionization state with $\xi < 1 \text{ erg cm s}^{-1}$, suggesting that the reflecting matter is located at some distance from the X-ray source: $\sim 0.75 \left(\frac{L^{\text{ion}}}{5 \times 10^{42} \text{ erg s}^{-1}} \right)^{1/2} \left(\frac{\xi}{1 \text{ erg cm s}^{-1}} \right)^{-1/2} \left(\frac{n}{10^6 \text{ cm}^{-3}} \right)^{-1/2}$ (pc). A characteristic broad-line region size (R_{BLR}) has been shown to be related to the X-ray, UV, and optical continuum luminosities (Kaspi et al. 2005). Using their relationship, the characteristic R_{BLR} was estimated to be $\sim 0.003 \left(\frac{L_{2-10}}{2 \times 10^{42} \text{ erg s}^{-1}} \right)^{0.7}$ (pc). The distance of the reflecting matter is larger than the characteristic size of broad line region of NGC 2273. It is natural to consider the reflection matter to be the dusty torus which also obscures the broad line region in this Seyfert 2 galaxy.

We tried to determine the properties of the dusty torus of NGC 2273 by fitting the reflection component seen in the observed spectrum with the reflection model based on simulations. Although the opening angle of the torus was poorly constrained, we found that we observe the nucleus along a line of sight intercepting the torus near its edge. If the photon index was fixed at 1.9, the intrinsic luminosity in the 2–10 keV band and the column density of the torus along the equatorial plane were estimated to be $1.9 \times 10^{42} \text{ erg s}^{-1}$ and $4.8_{-3.0}^{+5.2} \times 10^{24} \text{ cm}^{-2}$, respectively. The large column of the torus naturally explains the observed large iron line EW of 1.8 keV (e.g., Ikeda et al. 2008). However, the large column predicts a large fraction of CS up to 0.2 (e.g., Matt 2002). In the torus geometry, the column density should be small, and/or the opening angle should be large to obtain such a small CS. We performed Monte Carlo simulations using the torus geometry to explain the small CS. Figure 7 shows the fraction of the CS as a function of column density and opening angle. The large opening angle seems to be inconsistent with the small fraction of the scattering X-rays. To resolve the puzzle about the small CS, an accurate measurement of the CS using an instrument with high energy resolution, such as the X-ray micro-calorimeter onboard *Astro-H*, is crucial.

5. Conclusion

We observed the weak Compton-thick Seyfert 2 galaxy NGC 2273 with the Japanese X-ray satellite Suzaku, and detected hard X-rays above 10 keV. The flux in the 15–40 keV is about $1 \times 10^{-11} \text{ erg s}^{-1} \text{ cm}^{-2}$. First, the broad-band spectrum from 0.3 to 40 keV was fitted with thin-thermal plus reflection components. The best-fit photon index was found to be 1.5, smaller than the canonical value of Seyfert galaxies. We then added an absorbed power-law component to the model. When we fixed the photon index at 1.9, the absorbed column and intrinsic luminosity in the 2–10 keV band were found to be $1.5 \times 10^{24} \text{ cm}^{-2}$ and $2 \times 10^{42} \text{ erg s}^{-1}$, respectively. Our observation reveals the obscured nucleus of NGC 2273. The luminosity ratio, $L_{\text{X}}/L_{[\text{OIII}]}$, for NGC 2273 is similar to those for Seyfert 1 galaxies. This indicates that the photoionized region that is emitting the [OIII] lines is consistent with being powered by

the nuclear activity. For the soft X-ray emission below 2 keV, it could be represented equally well by thin-thermal emission or by a scattered emission model as seen in Mrk 3, and thus we could not obtain a conclusive result on the origin of the soft component.

A strong iron $K\alpha$ line with an EW of 1.8 keV was detected. To achieve such a large EW, the direct light must be blocked by thick matter with $N_{\text{H}} > 2 \times 10^{24} \text{ cm}^{-2}$. This column density is consistent with the spectral fitting using a model based on a Monte Carlo simulation. However, the large column density is inconsistent with the observed small fraction of CS of the iron $K\alpha$ line. We also detected a weak iron $K\beta$ line with a center energy of ~ 7.0 keV. From the properties of $K\alpha$ and $K\beta$ lines, we conclude that the iron emitting matter is in a low ionization states of $< \text{Fe VIII}$, which indicate that the iron emitting matter is located far from the X-ray source.

We fitted the hard X-ray emission with a reflection model based on a Monte Carlo simulation, assuming a simple torus geometry. Although the opening angle of the torus was not constrained well, it was found that we observe the nucleus along a line of sight intercepting the torus near its edge. The column density of the torus along the equatorial plane is $4.8_{-3.0}^{+6.2} \times 10^{24} \text{ cm}^{-2}$ if the photon index is fixed at 1.9.

The authors wish to thank the members of the Suzaku team for their operation of the satellite, and the members of the Suzaku HXD team for their effort on the NXB study of the HXD. We are very grateful to an anonymous referee for valuable comments and to Dr. K. Leighly for her careful reading of our draft. This study is carried out in part by the Grant support for Scientific Research of Ehime university (H.A.) and the Grant-in-Aid for Scientific Research (20740109 Y.T.) of the Ministry of Education, Culture, Sports, Science and Technology.

References

- Anders, E., & Grevesse, N. 1989, *Geochim. Cosmochim. Acta*, 53, 197
- Awaki, H. et al. 2008, *PASJ*, 60, S293
- Bassani, L., Dadina, M., Naiolino, R., Salvati, M., Risaliti, G., Della Ceca, R., Matt, G., & Zamorani, G. 1999, *ApJS*, 121, 473
- Bianchi, S., Miniutti, G., Fabian, A. C., & Iwasawa, K. 2005, *MNRAS*, 360, 380
- Cappi, M. et al. 1999, *A&A*, 344, 857
- Condon, J. J., Cotton, W. D., Greisen, E. W., Yin, Q. F., Perley, R. A., Taylor, G. B., & Broderick, J. J. 1998, *AJ*, 115, 1693
- Della Ceca, R., Severgnini, P., Caccianiga, A., Comastri, A., Gilli, R., Fiore, F., Piconcelli, E., Malaguti, P., & Vignali, C. 2008, *Mem. S.A.It.*, 79, 65
- Ferruit, P., Wilson, A. S., & Mulchaey, J. 2000, *ApJS*, 128, 139

- Guainazzi, M., Matt, G., Brandt, W. N., Antonelli, L. A., Barr, P., & Bassani, L. 2000, *A&A*, 356, 463
- Guainazzi, M., Fabian, A. C., Iwasawa, K., Matt, G., & Fiore, F. 2005, *MNRAS*, 356, 295
- Heckman, T. M., Ptak, A., Hornschemeier, A., & Kauffmann, G. 2005, *ApJ*, 634, 161
- Ikedo, S., Awaki, H., & Terashima, Y. 2008, accepted to *ApJ*(arXiv0810.3950)
- Ishisaki, Y., et al. 2007, *PASJ*, 59, S113
- Itoh, T. et al., 2008, *PASJ*, 60, S251
- Kalberla, P. M. W., Burton, W. B., Hartmann, D., Arnal, E. M., Bajaja, E., Morras, R., & Pöppel, W. G. L. 2005, *A&A*, 440, 775
- Kaspi, S., Maoz, D., Netzer, H., Peterson, B. M., Vestergaard, M., & Jannuzi, B. T. 2005, *ApJ*, 629, 61
- Kokubun, M., et al. 2007, *PASJ*, 59, S53
- Koyama, K., et al. 2007, *PASJ*, 59, S23
- Levenson, N. A., Heckman, T. M., Krolik, J. H., Weaver, K. A., & Życki, P. T. 2006, *ApJ*, 648, 111
- Londsdale, C. J., & Londsdale, C. J. 1992, *ApJ*, 391, 629
- Maiolino, R., Salvati, M., Dadina, M., Della Ceca, R., Matt, G., Risaliti, G., & Zamorani, G. 1998, *A&A*, 338, 781
- Matt, G., Fiore, F., Perola, G.C., Piro, L., Fink, H.H., Grandi, P., Matsuoka, M., Oliva, E., & Salvati, M. 1996, *MNRAS*, 281, L69
- Matt, G., et al. 1997, *A&A*, 325, L13
- Matt, G., et al. 1999, *A&A*, 341, L39
- Matt, G. 2002, *MNRAS*, 337, 147
- Mitsuda, K., et al. 2007, *PASJ*, 59, S1
- Moran, E. D., Barth, A. J., Kay, L. E., & Filippenko, A. V. 2000, *ApJ*, 540, L73
- Nakajima, H. et al., 2008, *PASJ*, 60, S1
- Nandra, K., George, I. M., Mushotzky, R. F., Turner, T.J., & Yaqoob, T. 1997, *ApJ*, 477, 602
- Palmeri, P., Mendoza, C., Kallman, T. R., & Bautista, M. A. 2003, *A&A*, 410, 359
- Petitpas, G. R., & Wilson. C. D. 2002, *ApJ*, 575, 814
- Ranalli, P., Comastri, A., & Setti, G. 2002, *A&A*, 399, 39
- Risaliti, G., Miolino, R., & Salvati, M. 1999, *ApJ*, 522, 157
- Sako, M., Kahn, S. M., Paerels, F., & Liedahl, D. A. 2000, *ApJ*, 543, L115
- Serlemitsos, P.J., et al. 2007, *PASJ*, 59, S9
- Takahashi, T., et al. 2007, *PASJ*, 59, S35
- Terashima, Y., Iyomoto, N., Ho, L. C., & Ptak, A. F. 2002, *ApJS*, 139, 1
- Ueda, Y. et al., 2007, *ApJ*, 664, L79
- Whittle, M. 1992, *ApJS*, 79, 49
- Yang, Y., Wilson, A. S., Matt, G., Terashima, Y., & Greenhill, L. J. 2008, *ApJ*, in press (arXiv0809.4656)
- Yaqoob, T., et al. 2007, *PASJ*, 59, S283

Table 1. XIS0 count rates of the detected sources

NAME	$N_{0.4-2\text{keV}}^*$ ($\times 10^{-3}$ c s $^{-1}$)	$N_{2-10\text{keV}}^*$ ($\times 10^{-3}$ c s $^{-1}$)
NGC 2273	2.5 \pm 0.2	8.7 \pm 0.4
2XMM J065012.9+604842	3.7 \pm 0.2	3.1 \pm 0.2
2XMM J065003.7+604639	2.9 \pm 0.2	1.1 \pm 0.2

* count rates within a $1'$ radius centered on each source

Table 2. Best-fit parameters of the three models to the wide-band spectrum of NGC 2273

ID	model*	N_{H1}^\dagger ($\times 10^{22}$ cm $^{-2}$)	soft component			hard component		χ^2 (d.o.f.)
			kT/scattering fraction (keV/ —)	abundance	photon index	N_{H}^\ddagger ($\times 10^{22}$ cm $^{-2}$)	R^\S	
1	T+R+lines	0.29 $^{+0.25}_{-0.15}$	0.59 $^{+0.20}_{-0.14}$	0.04 $^{+0.12}_{-0.03}$	1.49 $^{+0.13}_{-0.08}$			120 (120)
2	T+R+abs-PL+lines	0.30 $^{+0.28}_{-0.18}$	0.56 $^{+0.14}_{-0.16}$	0.05 $^{+0.17}_{-0.04}$	1.9 (fixed)	146 \pm 42	0.5 $^{+0.7}_{-0.3}$	119 (120)
3	S+R+abs-PL+lines	0.14 \pm 0.07	0.092 $^{+0.021}_{-0.018}$	-	1.8 (fixed)	115 \pm 40	0.8 $^{+1.2}_{-0.4}$	121 (122)

* T: thin thermal plasma model (*mekal*). R: cold reflection model (*peaxrv*). abs-PL: absorbed power-law emission. S: scattered emission.

† the absorption column for each model, i.e. $\exp(-\sigma N_{\text{H1}})$ (model).

‡ the absorption column for the absorbed power-law emission.

§ the reflection ratio of the cold reflection to the absorbed power-law emission.

Table 3. The best-fit center energy and intensity of each line in model 2

Center energy*	line width	intensity	EW	line identifications
(keV)	(eV)	($\times 10^{-6}$ ph s $^{-1}$ cm $^{-2}$)	(eV)	
0.745 $^{+0.045}_{-0.025}$	5 (fixed)	17 $^{+100}_{-14}$	75 $^{+440}_{-60}$	OVII RRC ($>$ 0.739 keV)
1.806 $^{+0.027}_{-0.025}$	10 (fixed)	1.7 \pm 0.7	160 \pm 70	Si K $_{\alpha}$ (1.740 keV) and Si XIII (1.854(f)/1.865(r+i) keV)
3.26 $^{+0.06}_{-0.14}$	10 (fixed)	0.9 $^{+0.7}_{-0.6}$	140 $^{+110}_{-100}$	Ar XVII (3.124(f)/3.140(r+i) keV) and Ar XVIII (3.32 keV)
6.400 \pm 0.005	4 ($<$ 26)	24.7 \pm 1.7	1810 \pm 120	Fe K $_{\alpha}$ (6.4038 keV)
7.06 \pm 0.03	4 ‡	3.2 \pm 1.0	270 \pm 85	Fe K $_{\beta}$ (7.058 keV)
7.50 $^{+0.09}_{-0.19}$	4 ‡	1.4 $^{+1.0}_{-1.1}$	130 $^{+90}_{-100}$	Ni K $_{\alpha}$ (7.4782 keV)

* corrected for cosmological redshift ($z=0.006138$).

† these line widths were linked to that of the 6.4 keV line.

Table 4. Best-fit parameters of the cold reflection model based on a Monte Carlo simulation

ID	model*	N_{H1} ($\times 10^{22} \text{ cm}^{-2}$)	soft component			hard component			χ^2 (d.o.f.)
			kT (keV)	abundance	photon index	N_{H}^\dagger ($\times 10^{22} \text{ cm}^{-2}$)	$\theta_{\text{oa}}^\dagger$ ($^\circ$)	$\theta_i^\dagger - \theta_{\text{oa}}$ ($^\circ$)	
4	T+RS+abs-PL+lines	0.39 (<0.9)	$0.75^{+0.25}_{-0.40}$	0.2 (<5)	$2.42^{+0.08}_{-0.57}$	540^{+370}_{-310}	40^{+25}_{-30}	$3 \pm 2^\ddagger$	108 (106)

* RS: cold reflection model based on a Monte Carlo simulation.

† N_{H} : the column density along the equatorial plane of the torus. θ_{oa} : the opening angle of the torus. θ_i : the inclination angle of the torus.

‡ the best-fit value and error are listed, when θ_{oa} is fixed at the best fit value.

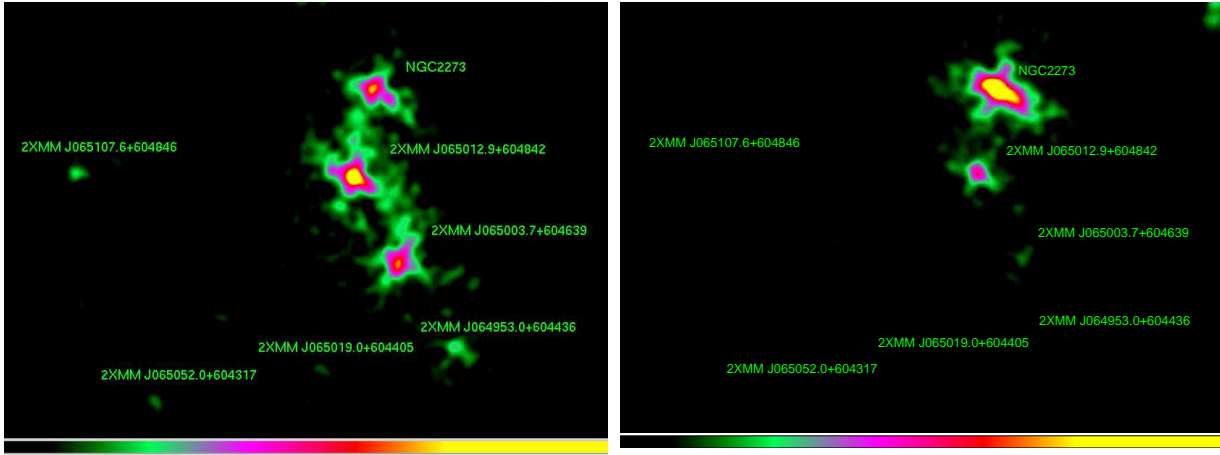


Fig. 1. The 0.4–2 keV (left) and 2–10 keV (right) images for NGC 2273 obtained by Suzaku. The images were smoothed by a gaussian function with $\sigma=0'.2$. The color scale is linear in the range of 0.013–0.413 c pix⁻¹ for the 0.4–2 keV image and in the range of 0.03–0.63 c pix⁻¹ for the 2–10 keV image. The minimum value for each image corresponds to the background emission.

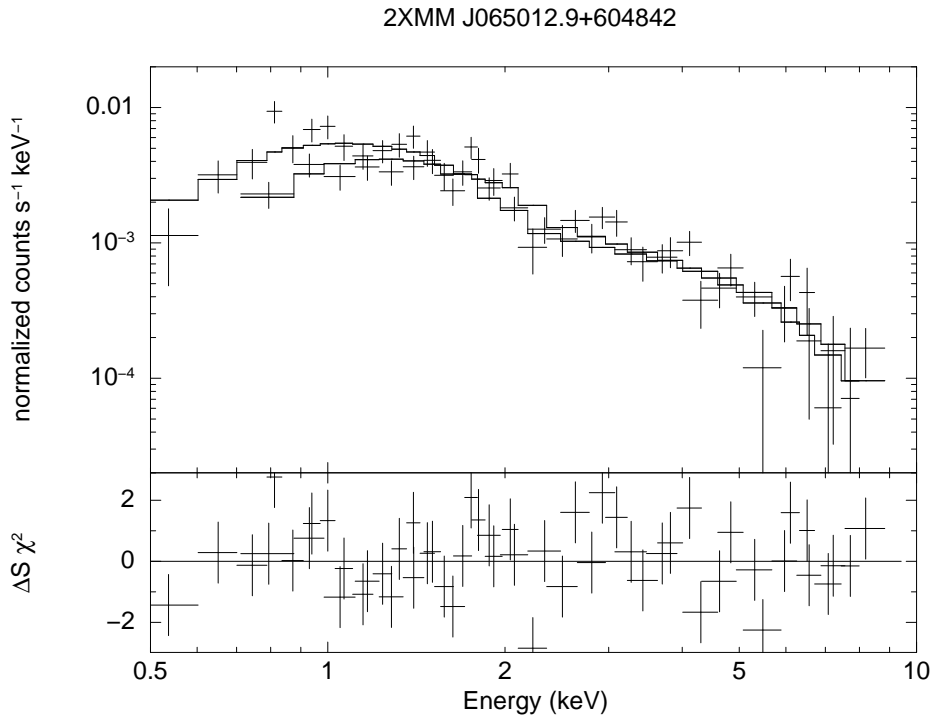


Fig. 2. The spectrum of 2XMM J065012.9+604842 observed with the Suzaku XIS. The spectrum is fitted with a single power-law model.

PIN 15–40 keV light curve

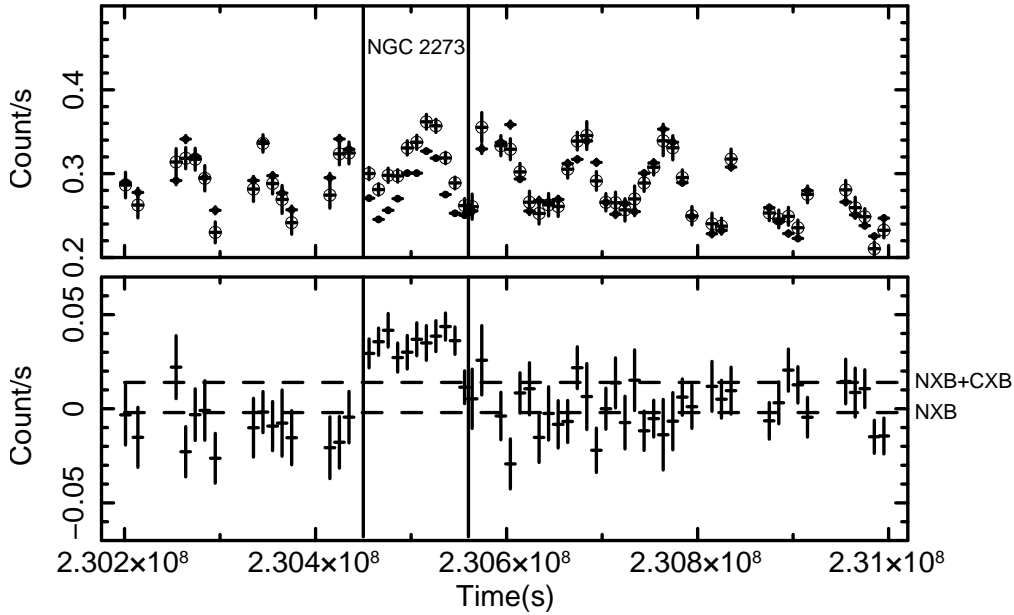


Fig. 3. The HXD PIN light curve in the 15–40 keV band. The upper panel shows observed count rates (open circles) and NXB count rates reproduced from the tuned NXB events (filled circles). The PIN light curve consists of data from earth occultation periods and the data from NGC 2273. The lower panel shows a light curve after NXB subtraction. The "NXB" in the lower panel shows the mean count rate of the earth occultation data after NXB subtraction. The CXB is the count rate of the cosmic diffuse X-ray background radiation in the 15 – 40 keV band, estimated to be 0.016 c s^{-1} .

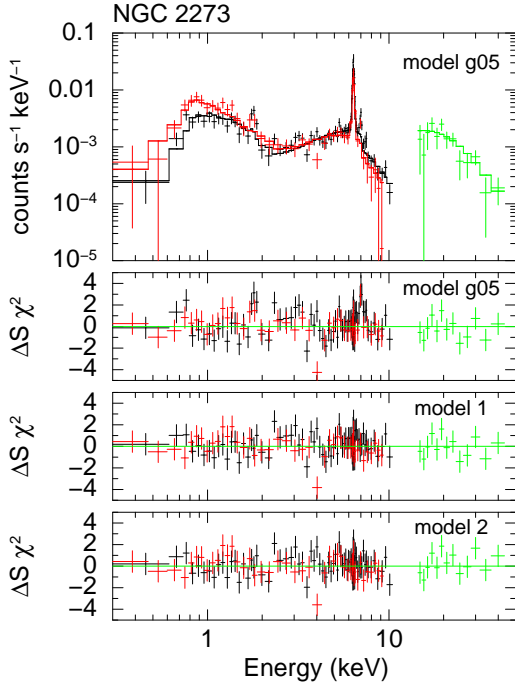


Fig. 4. A broad-band spectrum of NGC 2273 observed with Suzaku and residuals for our fitting models. The upper panel shows the wide-band spectrum obtained by XIS0+3 (black), XIS1 (red), and PIN (green). The "model g05" corresponds to the model by Guinazzi et al. (2005). Models 1 and 2 are described in Table 2.

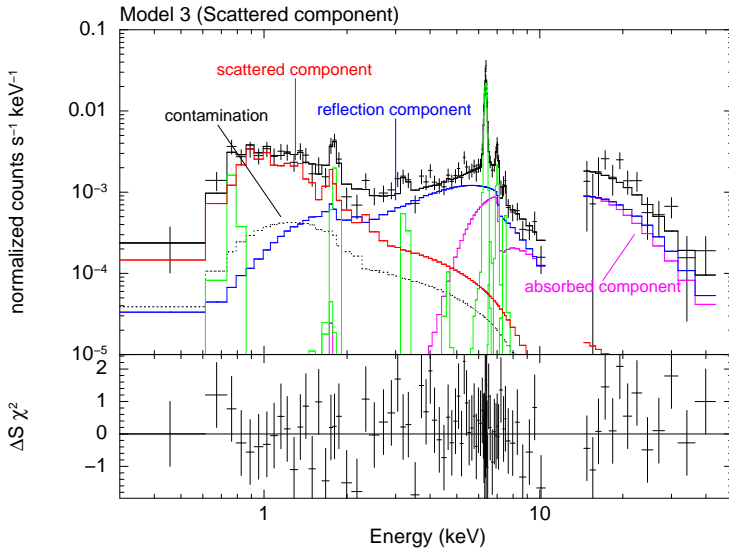


Fig. 5. The best-fit spectrum obtained by XIS0 and PIN for the model 3 in Table 2. In this model, the soft component was fitted with a scattered light. We also display the contamination (dashed line) from the nearby bright source (see text). The green lines indicate emission lines included in our fitting model. Escape lines for the emission lines are also displayed in this figure.

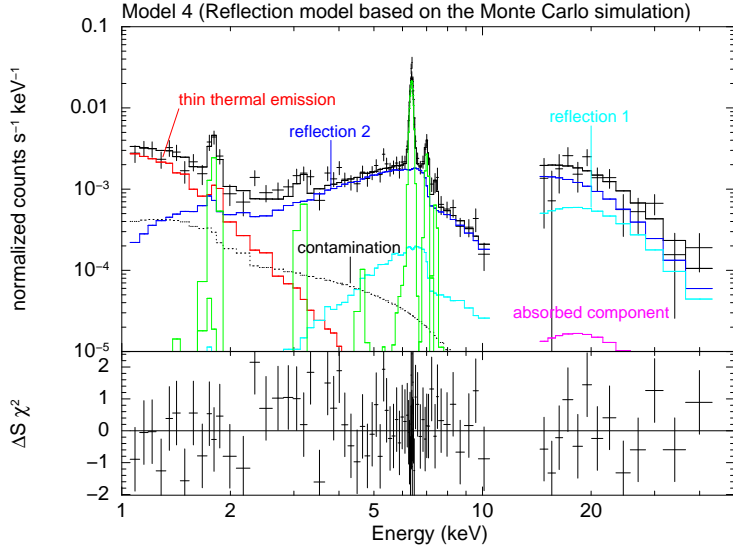


Fig. 6. The best-fit spectrum obtained by XIS0 and PIN for model 4 in Table 4. In this model, the reflection component was fitted with the reflection model based on a Monte Carlo simulation (Ikeda et al. 2008). A brief explanation of reflections 1 and 2 is presented in text. The green lines indicate emission lines included in our fitting model. Escape lines for the emission lines are also displayed in this figure. The photon index of the power-law emission from the central X-ray source is fixed at 1.9.

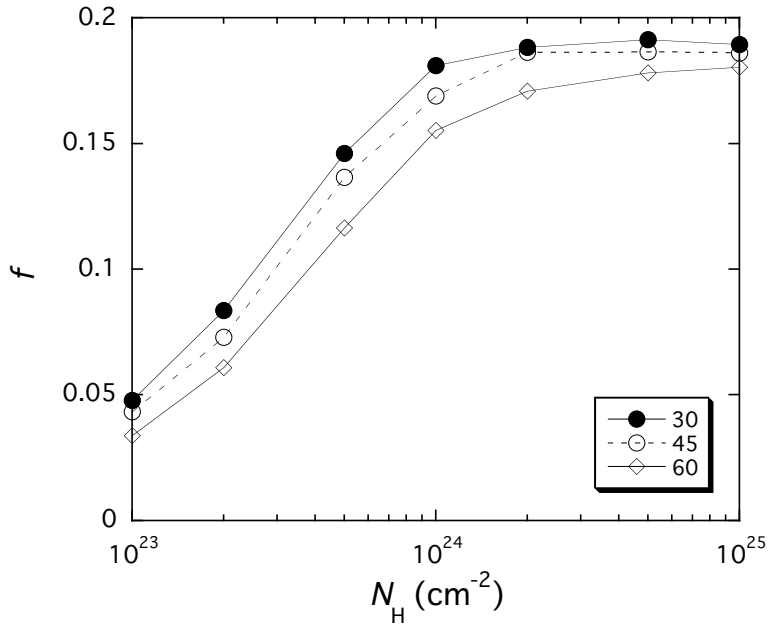


Fig. 7. Fractions of the Compton shoulder with respect to the primary gaussian component as a function of the column density along the equatorial plane of a dusty torus. The fractions for the opening angles of 30° (filled circles), 45° (open circles), and 60° (open diamond) were estimated from the Monte Carlo simulation developed by Ikeda et al. (2008). The photon index of the power-law emission from a central X-ray source is fixed at 1.9.